FULL PAPER

2D Materials Oxidation

NANO · MICRO

small

www.small-journal.com

Check for updates

New Concepts for Production of Scalable Single Layer Oxidized Regions by Local Anodic Oxidation of Graphene

Sergio J. Quesada,* Fernando Borrás, Miguel García-Vélez, Carmen Coya, Esteban Climent, Carmen Munuera, Ignacio Villar, Víctor A. de la Peña O'Shea, Alicia de Andrés, and Ángel L. Álvarez*

A deep comprehension of the local anodic oxidation process in 2D materials is achieved thanks to an extensive experimental and theoretical study of this phenomenon in graphene. This requires to arrange a novel instrumental device capable to generate separated regions of monolayer graphene oxide (GO) over graphene, with any desired size, from micrometers to unprecedented mm^2, in minutes, a milestone in GO monolayer production. GO regions are manufactured by overlapping lots of individual oxide spots of thousands μm^2 area. The high reproducibility and circular size of the spots allows not only an exhaustive experimental characterization inside, but also establishing an original model for oxide expansion which, from classical first principles, overcomes the traditional paradigm of the water bridge, and is applicable to any 2D-material. This tool predicts the oxidation behavior with voltage and exposure time, as well as the expected electrical current along the process. The hitherto unreported transient current is measured during oxidation, gaining insight on its components, electrochemical and transport. Just combining electrical measurements and optical imaging estimating carrier mobility and degree of oxidation is possible. X-ray photoelectron spectroscopy reveals a graphene oxidation about 30%, somewhat lower to that obtained by Hummers' method.

1. Introduction

The integration of a 2D material with its own oxide in multiple regions over the same single layer, at scale from tens μm to mm, is currently an unsolved issue. This has not only prevented the expansion of commercial applications in the field of plasmonics[1] and multianalyte sensor platforms,[2] but also the adequate characterization and in-depth study of the fundamentals of oxidation in 2D space.[3]

The difficulties to perform the optimum integration result from the almost opposing methods used by industry to supply both species. In case of graphene, commercial graphene oxide (GO) is supplied as flakes obtained by improvements of the original Hummers' method. It means they are typically processed in solution, which impedes the deposition in separated areas, as well as obtaining true 2D monolayers with mm extension. In contrast, the highest quality graphene single layers are manufactured by chemical vapor deposition (CVD) and are delivered transferred onto any substrate by a well automated process. Graphene flakes exfoliated by high power sonication of graphite are also provided as dispersion for solution processing. Graphene thin films (not single layer) are also obtained from previously deposited GO films by chemical reduction with different techniques (delivering the so-called reduced graphene oxide, rGO), but with poor quality compared with that of CVD monolayer graphene.[4] The inverse procedure, namely, electrochemical oxidation of graphene by local anodic oxidation (LAO) appears as a suggestive patterning technique to achieve a direct integration of single layers of both materials with the highest quality, optimal control, and precision.

In contrast to the variety of techniques using subtractive or additive methods to pattern graphene (conventional photolithography,[5] electron beam,[6] imprint-lithography,[7] dip-pen nanolithography,[8] inkjet printing[9,10]), those focused in generating a degree of oxidation over the material, like LAO, find the advantages of allowing, in one step, direct integration of insulating/conducting regions for devices and spatially tuning of chemical properties for subsequent reactions.

Dr. S. J. Quesada, F. Borrás, Dr. M. García-Vélez, Prof. C. Coya,
Prof. Á. L. Álvarez
ETSI Telecomunicación
Universidad Rey Juan Carlos
C/ Tulipán, Móstoles 28933, Spain
E-mail: sergio.quesada@urjc.es; angelluis.alvarez@urjc.es
Dr. E. Climent
ETSI Industriales
Universidad Politécnica de Madrid
C/ José Gutiérrez Abascal, Madrid 28006, Spain
Dr. I. Villar, Dr. V. A. de la Peña O'Shea
Photoactivated Processes Unit
Instituto IMDEA Energía
C/ Ramón de la Sagra 3, Móstoles 28935, Spain
Dr. C. Munuera, Prof. A. de Andrés
Instituto de Ciencia de Materiales de Madrid – CSIC
Cantoblanco, Madrid 28049, Spain

**ADVANCED
SCIENCE NEWS**
www.advancedsciencenews.com

**NANO · MICRO
small**
www.small-journal.com

Focusing on the patterning techniques which play with oxidation/reduction processes, LAO is a direct-writing method with an accurate and versatile positional control, what represents an advantage over those oxidizing techniques requiring previously manufactured templates.[11,12] The low-cost and simplicity of the scanning probe used to perform LAO contrasts with the complexity of the procedures using nanopipettes or complex electrochemical cells.[13,14] In this context, LAO is an environmentally friendly method based on controlling ambient humidity instead of using chemicals (occasionally very aggressive with the environment, like hydrazine, etc.). Some techniques, like hot tip lithography or laser treatments, are restricted to operate inversely by reducing GO multilayer films,[15,16] delivering graphene of significantly lower quality than that obtained by CVD. As will be shown, voltage and contact time are two operative parameters of LAO which provide control over the size of the oxidized spots in a more accurate way than a hot tip or a laser can do. Ultimately, LAO of graphene can be scaled in a very wide range, from nano- (using scanning probe microscopes)[17] to micro- and millimeters, as will be shown in this work.

In bulk materials, anodic oxidation is a 3D phenomenon, which progresses in vertical and horizontal directions.[17–22] In the vertical direction, the oxidized region extends above and below the surface baseline. This process has been exhaustively modelled according to modifications of the original concepts proposed by Cabrera and Mott.[23–25] The lateral expansion of the oxidized region, however, has been studied to much lesser extent. It is accepted that is restricted to the dimensions of the water meniscus promoted by the high electric fields (about 10^9 V m^{-1}) below the probe apex under voltage application.[26,27] With negative polarity, oxyanions are pushed toward the grounded electrode surface being responsible for its oxidation. The water bridge should remain very close to the probe due to the sharp decay of the electric field in the horizontal direction beyond the tip.[28,29] So it has been indeed observed for fast pulse voltages (<15 V in the order of tens of ms). But for longer exposure times (up to s), a lateral expansion of a very thin oxide layer is actually evidenced, which progress unavoidably, spoiling the aspect ratio of the features.[30–34] In fact, it will be confirmed later that the disc-shaped oxidized region in graphene expands much more than expected according to the estimated dimensions of the water meniscus around the tip.[35,36]

A decade ago, LAO of graphene began to be developed through scanning probe techniques in conditions similar to those practiced on Si (operating voltage usually < 15 V),[37,38] and, more recently, on 2D transition metal dichalcogenides.[39,40] Features such as dots and stripes produced by LAO have been manufactured previously with scanning nanoprobes (AFM), and the behavior with variable voltage, probe speed or humidity has been described qualitatively in just a few works.[41–43] However, to date no exhaustive studies have been carried out to explain the dependence of the oxide expansion with the operating parameters, as will be shown in the present work.

Since LAO is performed in series (point after point) and almost exclusively with scanning nanoprobes, the slow working speeds severely limit the scalability. One of the purposes of this work is to overcome this limitation with a new experimental setup, to achieve large oxidized sizes, higher operating speeds,

and scale the process to large areas, from µm to mm. This has enabled unprecedented characterization by Raman and X-ray photoelectron spectroscopy (XPS), as well as recording the electric current during the process. Ultimately, these observations have allowed us to fulfill the main objective: to formulate an oxidation model from physical first principles, which explains well the trends of the experimental curves and can be extended to other 2D materials.

In next sections, we study the formation of the GO fingerprint with operating conditions such as voltage, relative humidity and exposure time, to elucidate the mechanisms driving the process (Section 2.1). The hitherto unobserved transient electrical response during LAO of graphene is recorded and interpreted (Section 2.2). The observations provide the keys to propose a new driving mechanism for the oxidation process, previously unnoticed in LAO over 3D materials. The oxidation progress is then modelled from classical first principles (Sections 3.1–3.3). With the aid of this formalism, we will discriminate the different current components (transport or electrochemical) present in the electrical response during LAO (Section 3.4). Finally, as a matter of proof, we accomplish the milestone of manufacturing large area substrates of combined high-quality graphene and monolayer GO patterns, with sizes of several mm^2 and a detailed characterization of the C molecular bonds by XPS.

2. Results

2.1. Evolution of the Oxide Propagation in Graphene with Operating Conditions

Under appropriate conditions of humidity and voltage, oxidation has been performed by approaching the tip to graphene until making a single contact and next separating the tip, while a constant voltage is hold along the process. If the voltage is applied after the tip contact (as usual with nanoscopic probes), the tip will dislodge moisture between it and graphene, many points of the tip metal come into close contact with the sample, establishing an electrical contact (ohmic/schottky) leading to constant conduction and no oxidation.

Figure 1a shows, at the same scale, two single spots generated when we apply our procedure at a fixed V_0 but in very different RH conditions. In this case graphene is on a SiO_2/Si:p$^+$ substrate. In both differential interference contrast (DIC) images, the main feature and that at the inset were performed at $V_0 = -50$ V and a contact time between tip and graphene of 0.24 s. The large circular shape of the spot generated at RH = 75%, which we will recognize below as oxidized graphene, contrasts with the much smaller and, above all, irregular shape of the "crater" obtained in dry conditions (inset). The white dashed circle at the center of the large spot represents an estimation of the tip size. Craters generated at low RH < 40% usually exhibit a brighter contrast due to the removal of graphene (as confirmed by the disappearance of the Raman signal), and appear to progress not radially but through lobes or fingers, indicating that are driven by a different mechanism.[44] For more information about results of craters by graphene removal, see the Supporting Information.
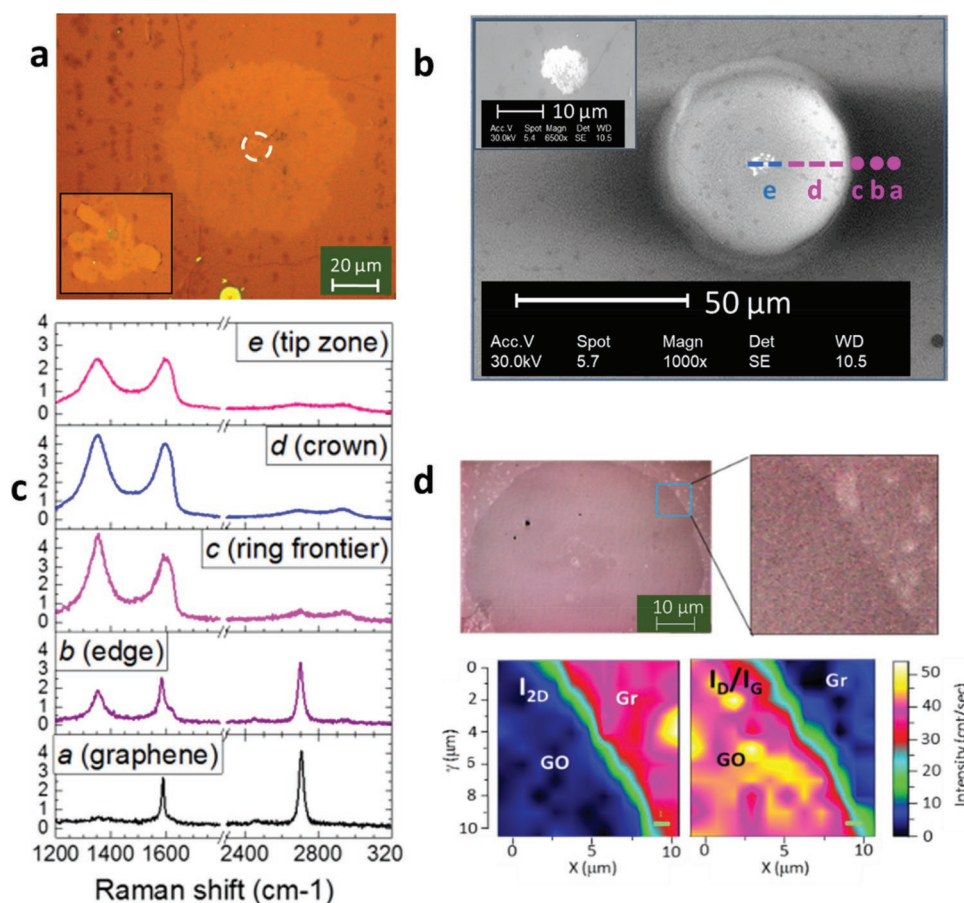
ADVANCED
SCIENCE NEWS
www.advancedsciencenews.com

NANO · MICRO
small
www.small-journal.com

Figure 1. a) Circular feature obtained on graphene/SiO$_2$/Si:p+ at −50 V, exposure time 0.24 s, and RH = 75%. Inset shows, at same scale, a graphene spot at identical operating conditions but RH = 33%. b) SEM image of the oxidized spot performed on graphene/quartz at −25 V with RH = 94% and 30% (inset). c) Raman spectra recorded from the marked points, and average spectra recorded from the dotted lines marked in (b). d) Images of a GO spot on graphene/quartz at −25 V and RH = 94% and Raman maps of I_{2D} and I_D/I_G ratio in a square of 10 × 10 µm close to the edge of the spot.

The large size acquired by the spots is a great novelty that allows evaluating their composition and uniformity inside. The regular, circular and large size characteristic of the spots obtained at high humidity, and the irregular and smaller size of those craters generated in dry environment are general observations, regardless of substrate and applied voltage, if sufficiently high ($|V_0| > 20$ V). This characteristic is illustrated in Figure 1b and subsequently in Figure 3 for a variety of voltages and humidity levels. Figure 1b shows a similar feature obtained on graphene transferred onto quartz, carried out at different conditions ($V_0 = -25$ V and RH = 94%), in this case characterized by secondary electron microscopy (SEM) imaging. The clear contrast of the circular disc in the SEM image indicates its insulating character respect to the dark background from the semimetallic graphene. The inset in the upper left corner shows the ellipsoidal fingerprint left by the tip at same voltage but in dry atmosphere (RH = 33%). The bright zone in the center of the disc (just slightly smaller than the probe fingerprint of the inset) is precisely attributed to the contact with the tip, and will be analyzed below. The rest of the disc is rather uniform, although dotted with small dark points of 1–2 µm size, spread randomly and also present in the pristine graphene. These dots are identified as second layer nucleation islands, a typical

feature of graphene grown by CVD. Close to the edge, the wide ring (4 µm) of gradual contrast is mainly attributed to an artifact from the space charge build up at the insulator/conductor edge (see the Supporting Information).

To investigate the nature of the described features, micro-Raman spectra have been recorded from different regions of the spot. Figure 1c shows representative spectra recorded along the points and dotted lines marked in Figure 1b. The spectrum a corresponds to the outer zone of pristine graphene, and exhibits the first order "G" graphene mode at 1580 cm^{-1} and the second order 2D at 2700 cm^{-1}, whose shapes and relative intensities indicate a high-quality monolayer. At point b, a transition spectrum shows the above modes superimposed with broad peaks from the inner region. This occurs when the 0.7 µm laser spot excites both the pristine graphene and the edge of the disc. Spectrum recorded from point c is representative from the ring zone close to the border. Here, Raman scattering from the monolayer GO reveals the features traditionally associated with graphene oxide in thin films: a broad an intense D defects peak (≈1350 cm^{-1}), a broadened graphene G peak with a high energy shoulder (≈1620 cm^{-1}) attributed to the D' mode,[45] and especially the drastic decline of the 2D band. Further inside (circular crown), spectrum d shows an average

ADVANCED
SCIENCE NEWS
www.advancedsciencenews.com

NANO · MICRO
small
www.small-journal.com

of 12 single spectra recorded along the dotted line between the tip-affected central region and the ring frontier. Although these Raman modes arise from scattering by sp^2 C bonds, and not directly from C—O bonds, the relationship between their width and relative intensity (I_D/I_G) has been closely correlated with the degree of oxidation. The full width at half maximum (FWHM) of D band in the individual spectra is ≈75 cm⁻¹. The I_D/I_G intensity ratio is between 1.1 and 1.3, and FWHM of G band is ≈90 cm⁻¹. The study of de Andrés et al. on partially reduced GO shows that these Raman parameters points to a high degree of oxidation.[46,47] Further information will be obtained from XPS spectra (Figures 8c,d, see below). The edge of the spot and the uniformity of the GO are better visualized in the Raman maps recorded from regions of 10 × 10 μm, shown in Figure 1d (for both the 2D band intensity and the I_D/I_G ratio), where the uniformity of the oxidation is evident (contrast is enhanced by colors). Finally, spectrum e in Figure 1c is an average of 8 spectra recorded from different points along the line crossing the bright central region affected by the tip. This region exhibits flattened peaks with half the intensity of the corresponding spectra from the GO crown. In view of the brighter contrast provided by SEM images, these regions can be considered more insulating. Here, oxidation was likely accomplished on a region of cracked graphene, where the 2D lattice can be removed at a few scattered points, what justifies a reduction in the overall intensity.

Figure 2 shows atomic force microscopy (AFM) carried out on a representative spot among those performed at $V_0 = -25$ V and RH = 94%, in graphene transferred onto quartz. Simultaneous topographic (Figure 2a) and electrostatic (Figure 2b) images are recorded using electrostatic force microscopy (EFM) mode. The location of the GO disc is clearly visible in the electrostatic image, presenting a brighter contrast than the surrounding nonmodified graphene. This is in clear contrast to the topographic image, where no appreciable differences between modified and unmodified graphene are measured. Figure 2c,d shows higher magnification images at the disc edge, with the corresponding line profiles along the border. Among the predominant features in the topographic profile are clusters ≈3–4 nm high, corresponding to ambient adsorbates that cover the entire graphene surface, and explain the residual oxidation detected later on non-treated graphene (see the Supporting Information). Particularly relevant for the present work is the absence of damage or changes in the graphene layer after the GO formation, presenting an almost indistinguishable morphology between the pristine and GO regions. The clear contrast between zones observed in the corresponding EFM images is thus the only evidence of graphene modification when characterized with AFM. Several groups have reported the use of EFM mode to characterize graphene-based materials,[48–50] showing that EFM contrast arises for graphene presenting different degrees of oxidation.[51]

In order to study the mechanisms governing the GO formation, we firstly focus on the influence of the operating voltage on the GO size. Series of spots have been performed in graphene/quartz at different voltages (from −15 to −60 V at probe) and RH values from 40% to 99%, keeping constant the duration of the contact between tip and graphene at 0.24 s. As an example, **Figure 3**a shows a DIC image captured on those GO
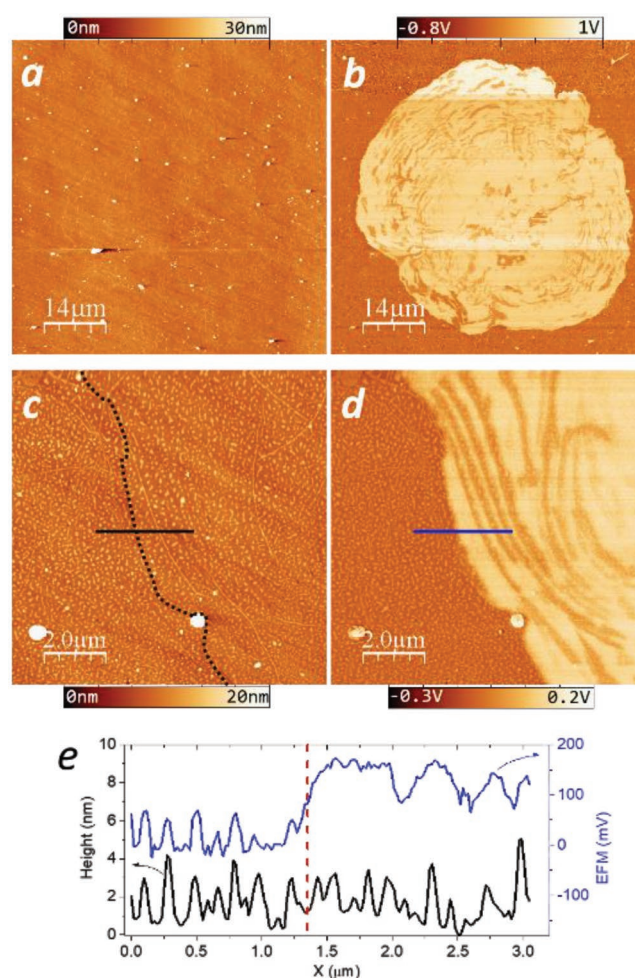

Figure 2. a,c) Simultaneous topographic and b,d) electrostatic images recorded in EFM-mode on a GO spot, performed at $V_0 = -25$ V and RH = 94% in graphene/quartz. The dotted line in (c) marks the spot edge. e) Profiles taken at the marked lines in (c) and (d), along the spot edge. Red dotted vertical line marks the position of the spot border.

spots performed at RH = 99%, with operating voltage from −25 to −45 V. We highlight the regularity both in size and in circular shape of the points within the same row, particularly those generated at higher voltages.

The evolution of the GO mean radius, r_{GO}, normalized to the tip radius, r_0, with increasing $|V_0|$ is shown in Figure 3b, for a chosen range of RH values to provide a scope of dots with r_{GO}/r_0 from 1 to 10. Each point averages the size of the five spots in a row, the error bar being the calculated standard deviation. Solid curves represent the fit to an electrostatic model explained in Section 3.3. For RH ≤ 70% and $|V_0| > 30$ V, the processes of cracking and removal of graphene clearly interfere with the progress of the oxidation, eventually perturbing a right determination of the spot size. When removal of graphene dominates the process, and irregular craters are generated, an effective radius (r_{eff}) can be still defined as that of the circle having the same area. In this case, the evolution of r_{eff} with voltage shows a considerably lower slope than that
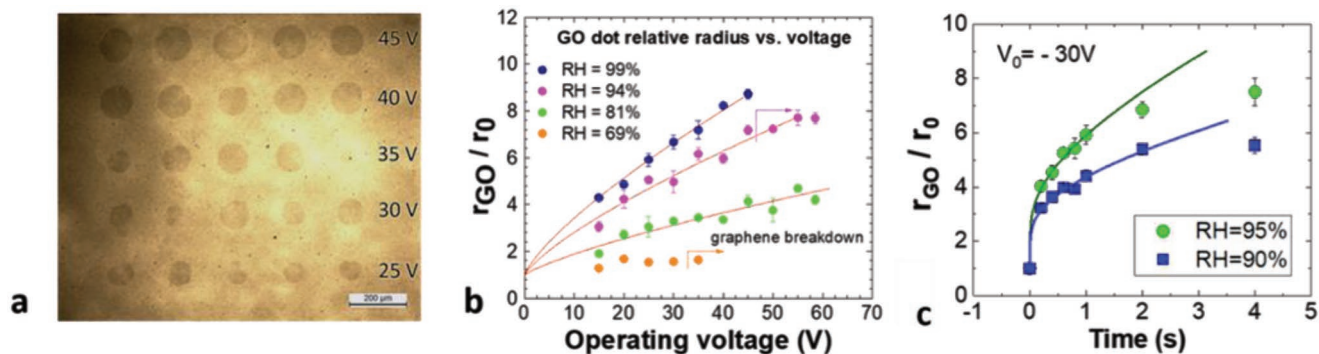
Figure 3. a) Optical image of GO circular spots performed on monolayer graphene/quartz, at different voltages (from −25 to −45 V) in saturated 99% relative humidity. b) Evolution of the GO dot radius r_{GO} (normalized to the tip radius, $r_0 = 6.3$ μm) with increasing operating voltage at four different RH values. c) Evolution of the relative radius (r_{GO}/r_0) of the GO spots as the contact time between tip and graphene (exposure time) is prolonged. Operative voltage is −30 V and two sets were recorded at RH = 95% (circles) and RH = 90% (squares). Error bars result from the average of several spots. Solid lines are the fit to an oxide growth model.

observed for the GO spots in Figure 3b (see the Supporting Information).

To complement the previous studies, series of oxidations have been performed to track the progress of the spot size with the exposure time for fixed operating voltage ($V_0 = -30$ V) and two high RH values, 95% and 90%. These high RH values are optimal for observing clear trends until longer times, with less interference from extrinsic defects.

The points of Figure 3c represent the relative radius, r_{GO}/r_0 measured for a discrete set of contact times between tip and graphene (from 0.1 to 4 s). Solid curves represent the fit to an oxide growth model explained in Section 3.3. These curves are very relevant since the area of each spot is proportional to the incorporated oxyanions, and the evolution along time should keep a close relation with the current traces $I(t)$ recorded during oxidations, in particular, with the integral of theses traces, as explained in the next section. The tendency reveals a very fast grow during the first 20 ms, contrasting with a slowing down from the tenths of a second onward.

Summarizing, the evolution of the spot relative radii with operation voltage for a constant exposure time can be considered quasilinear in a wide range of RH values, only exhibiting a nonlinear tendency for low electric fields ($|V_0| < 15$ V), which is more clearly evidenced at high RH (Figure 3b) due to the large spot size. The nonlinearity is, however, very pronounced with exposure time for a fixed voltage, especially for $t < 20$ ms. In this range, the slope is very fast, what causes greater difficulty in obtaining reproducible features, unless a very precise control system is available. On the other hand, spots recorded using long exposure times (>2 s) often show an irregular shape, an indication that for larger sizes the driving force of the process is more easily obstructed by random defects. Ultimately, increasing RH slightly prevents the formation of electric shocks during the approach of the probe to graphene (as will be shown later) and, therefore, helps to preserve a correct oxidation to higher voltages without graphene breakdown. The lateral expansion of oxidation appears as a quite different phenomenon to that produced in the vertical direction. It obeys other rules, which will be elucidated below, and can be applied to explain oxidation behavior (anisotropy, etc.) in any 2D material

2.2. Electrical Traces Recorded During Oxidation

Figures 1 and 3 illustrate the great difference between dry spots and those generated under sufficient humidity conditions. The differences in the mechanisms governing both types of footprints are more evident when the electrical response is measured during the process. This has been done by recording over time the voltage drop across a resistor in series with the probe, using a high sampling rate oscilloscope.

A representative current trace recorded during LAO of graphene at $V_0 = -30$ V and RH = 92% is shown in **Figure 4**. The process exhibits a full width at half maximum (FWHM) of a few tens ms, eventually decaying very slowly until the probe takes off. The capture of the weak current during LAO signals required the use of analogue electrical filters to suppress the DC voltage component and reduce the resistor thermal noise.
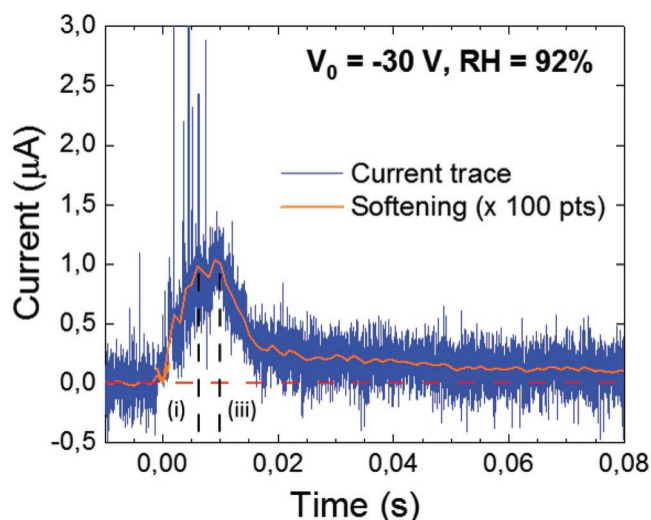

Figure 4. Current trace recorded during local anodic oxidation of graphene using $V_0 = -30$ V at RH = 92% (blue line). Orange solid line a softening from an average each 100 points. Baseline marked with dashed red line.
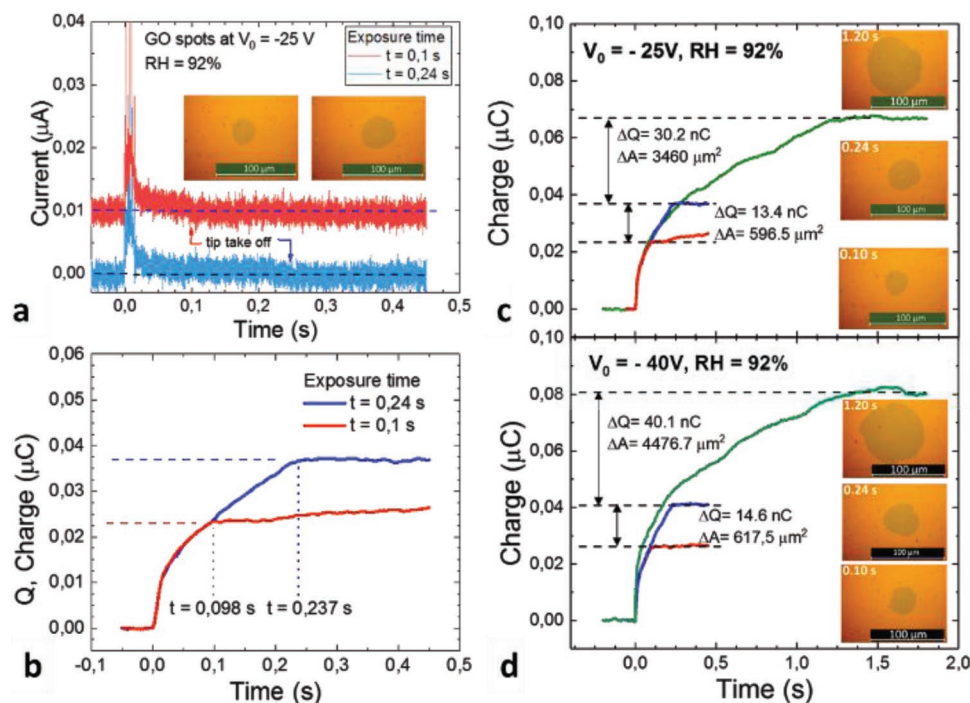
ADVANCED
SCIENCE NEWS
www.advancedsciencenews.com

NANO · MICRO
small
www.small-journal.com

Figure 5. a) Current traces recorded along oxidation of two spots at same operating voltage (−25 V) and relative humidity (RH = 92%). The oxidations were interrupted in the moments marked by the arrows. Insets show pictures of the spots at the same scale. b) Integral over time of both current traces, where the tip take off appears as a stabilization of the charge involved. c) Time integrals of the currents recorded during generation of three GO spots at −25 V and RH = 92% with different contact times: 0.1 (red), 0.24 (blue), and 1.2 s (green) (final spot size in insets). The legends indicate the charge and area increments from one spot to the other. d) Idem for three GO spots performed at −40 V with different contact times: 0.1 (red), 0.24 (blue), and 1.2 s (green) (final spot size in insets).

As far as we know, it is the first time these measurements have been reported in graphene.

Generally, three stages shown in the figure can be distinguished in the electrical traces: i) The initial monotonic increase of the current is attributed to the field increase as the gap between tip and graphene is reduced. The duration of this stage is <10 ms in all the traces recorded. Considering the speed and measured deceleration of the probe (0.3 mm s^{-2}), this gap corresponds to the last stretch of ≈7 nm before touching graphene. Note that during this stage the current appears dotted with very fast sparks of typical duration <1 µs, attributed to occasional thermoelectric ruptures (detailed in the Supporting Information). A few sparks, although more intense, are the only electrical features observed during the graphene removal produced at low RH. At high RH, defects resulting from these sparks are responsible for the bright contrast observed by SEM at the center of the spots (Figure 1b) coinciding with the projected area of the tip, and may play a relevant role as seeds for attaching the first oxyanions. ii) During a brief interval, the tip comes into contact with the sample, the electric field no longer increases, and the current flattens. In this stage, sporadic sparks may still appear. Since the sparks momentarily deactivate both the electric field and the capacitive effect, we consider that so far the oxidized area has grown scarcely, and then coincides approximately with the tip projection. iii) In the third stage, time for expansion of the GO disc begins to count and the current reduces gradually. In this interval, no sparks are observed that would interfere with the expansion. The

increment of the spot radius over time, as well as the evolution of the current trace, can then be studied clearly, and will be the subject of modeling in the Section 3.

During this stage, the current shows a fast decay along the first 10–20 ms, from which slows down indefinitely. This trend truly resembles that observed during LAO of Si by Dagata et al.,[34] empirically simulated by a two-exponential behavior with fast and slow time constants. However, during GO formation the equivalent time constants would be one order of magnitude shorter, and the relative expansion of the spots several times longer. Note that if we compare the time scale with that of Figure 3c, we conclude that most of the GO expansion is produced along this stage.

Figure 5a displays the currents measured along two oxidations, both performed at $V_0 = −25$ V and RH = 92%, but taking the tip off at 0.1 and 0.24 s, respectively. Colored arrows indicate the moment when the tip takes off for both traces, which are followed by a current interruption. The upper curve is displaced for convenience, but the dotted lines represent the corresponding background level for each one. The inset shows the resulting DIC images of both spots, with measured areas of 811 and 1407 µm^2 for the shorter and longer exposure times, respectively. Note that such a significant difference in area occurs in an interval where the difference in current is apparently not very high.

A quantitative analysis of the charge involved in the process, $Q(t)$, is provided by the time integral of the current traces. Integration appears as a powerful tool to suppress white noise and hence reveals interesting features, such as the moment

ADVANCED
SCIENCE NEWS
www.advancedsciencenews.com

NANO · MICRO
small
www.small-journal.com

when the tip is disconnected from graphene, stopping the charge increase (times marked in Figure 5b). At those times the spots also stop growing and acquire their final size. The plots $Q(t)$ also allow an accurate determination of the increments of charge $\Delta Q_{1,2}$ involved in the intervals $(t_2 - t_1)$, where the difference in current is apparently not very high (legends of figure 5b–d). Thus, one can propose equations such as

$$Q(t_1) + \Delta Q_{1,2} = Q(t_2) \tag{1}$$

which will serve below to derive easily some unknown parameters in the $Q(t)$ model.

The integrals along time for the current traces of Figure 5a (red line for the spot with the shorter exposure time and blue line for that with the longer) are plotted in Figure 5b. It can be observed how the charge of both processes evolves almost identically until $t = 0.095$ s, when the tip is disconnected from the smaller spot (red line), and the involved charge achieves a constant value of $Q = 23$ nC. The charge involved in the other spot (blue line) gets constant 140 ms later, at $Q = 37$ nC.

This charge may be correlated with that required to form the GO spot by the incorporation of oxyanions from the humid environment. If we assume that each incorporation would deliver one elementary charge, e^-, to the circuit (as in the case of OH^-),[52] it results striking to check that the charge difference between the integrated curves of the spots in Figure 5b, is much greater than that required to justify the increment of area from the smaller spot to the larger. In this case, the e^- involved are fourfold the number of C atoms in the area increment. This is a general result in our experiments for the interval 0.1–0.2 s, indicating that other current component apart from the electrochemical is acting and dominating the process in this interval. We attribute it to carrier transport or drift current assisted by the external electric field. In contrast, when the sampling interval extends from 0.2 to 1.2s, the number of electrons involved approaches that of the C atoms in the incremented area. This reveals that the drift component of the current tends to vanish as the size of the GO grows, while the electrochemical current, although slowly, still contributes to the expansion and tends to dominate in the long term.

The whole involved charge in different oxidation processes at −25 and −40 V are shown in Figure 5c,d, respectively, where the tip was detached to stop the oxidation at 0.1, 0.24, and 1.2 s. The insets show pictures of the final spot size acquired until those times.

For a specific V_0, the same arguments used above for Equation (1) can be applied within each group of $Q(t)$ curves to obtain a set of equations. If we count with a theoretical model for $Q(t)$, these equation systems may be used advantageously to derive the unknown parameters by simple algebraic methods. Next, a model describing the oxidation process is proposed, where $I(t)$ and eventually $Q(t)$ are formulated.

3. Discussion

One of the objectives of this work is to offer a mathematical formulation for the progress of the GO spots, sufficiently general so that it can be extended to the oxidation of other 2D materials. The previous observations on the oxidation of graphene will serve as the basis for this model. For this purpose, we choose the simplest conceptual tools, similar as those used in the Mott-Cabrera model for metal oxidation.[25] In that model, the authors were concerned by two questions: i) How an oxygen ion could pass from the surface with the air to the metal interface making hops through the oxide layer. ii) What was the force driving the process (definitely, the electric field derived from the difference in electrochemical potential, either modified by any effect of strain or accumulation of space charge). In our case, three hypothesis greatly simplify the problem: i) The electric field is imposed externally by the constant voltage applied between the probe and the electrically grounded graphene. ii) The oxyanions do not have to travel through the oxide region, but just to incorporate at the perimeter between the already oxidized zone and the pristine graphene. iii) The oxidation expansion can be considered just a bidimensional problem, neglecting the deposition of a 2nd or subsequent oxyanion layers.

In this framework, we describe step by step the mathematical modeling for the graphene oxide expansion.

3.1. Determination of the Electric Field at the Boundary Between the Dielectric GO and the Semimetallic Graphene

In order to model the progress of the relative radius $\check{r} = r_b/r_0$ of a GO spot with the operating voltage we propose the 2D electrostatic geometry sketched in **Figure 6**, where we distinguish three zones: i) Contact of the metallic tip with the layer, represented by an inner metallic circle of radius r_0 (at potential $-V_0$). ii) The dielectric graphene oxide, represented by the circular crown between r_0 and r_b (edge). iii) The outer graphene beyond the GO crown, simplified as a perfect metal electrically grounded.
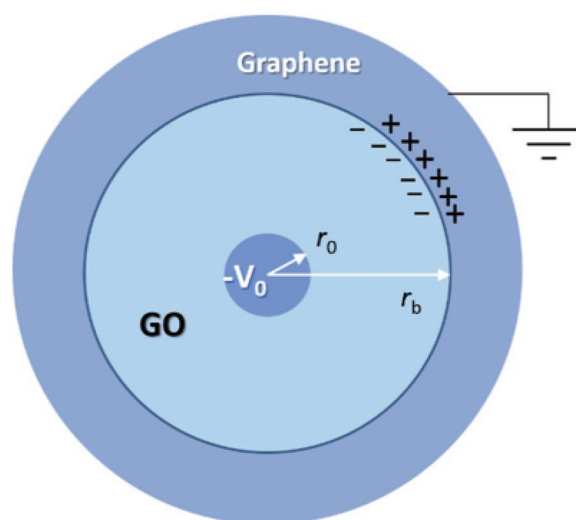

Figure 6. Plot of the 2D geometry formed by the tip footprint (idealized as the inner circle with radius r_0) polarized at voltage V_0, circular crown of graphene oxide (from r_0 to r_b), and graphene electrically grounded at the outer zone.

In the pure 2D space proposed in Figure 6, the Laplace equation with radial symmetry and boundary conditions ($V(r_0) = V_0$ and $V(r_b) = 0$) has a straightforward analytical solution, where the potential $V(r)$ scales exclusively with the radius logarithm, and the electric field $E(r)$ with the radius inverse

$$V(r) = \frac{V_0}{\left(1 - \ln\left(\frac{r_0}{r_b}\right)\right)}\left(1 - \ln\left(\frac{r}{r_b}\right)\right) \tag{2}$$

$$\vec{E}(r) = \frac{V_0}{\ln\left(\frac{r_b}{r_0}\right)} \cdot \frac{1}{r}\vec{u} \tag{3}$$

where **u** is the radial unit vector. See the Supporting Information for further discussion about electrical permittivity, ε_r, in low dimensionality problems and validity of the 2D approach in our system.[53–56]

Labeling the electric field at the boundary GO/graphene as E_{GO}, the relative GO radius ř may be expressed from Equation (3) as a function of the applied voltage V_0 and E_{GO}

$$\check{r}\ln\left(\check{r}\right) = \frac{V_0}{r_0 \cdot E_{GO}} \tag{4}$$

The red solid lines in Figure 3b are fits to Equation (4) of the different series of GO radius versus applied voltage at a particular RH, where E_{GO} has been considered a fitting parameter. In view of the good fits, the dependence of r_b/r_0 on the operating voltage results consistent with a view in which the final electric field at the edge of all the GO spots performed at different voltages is unique for each RH. The underlying idea is that during anodic oxidation of graphene, the GO circles will expand until the electric field at the GO/graphene boundary drops to a critical value, E_{GO}, determined by RH and the duration of the tip-graphene contact. For a fixed exposure time, the higher the value of RH, the larger the spot size, what means that expansion is faster.

In our case, for an exposure time of 0.24 s, the critical boundary field E_{GO} obtained from the fits ranges from 3.4×10^5 to 1.3×10^6 V m^{-1} as RH decreases from 99% to 81%. The E_{GO} becomes lower, what means that the spot extends further, when more oxyanions are available in the environment (higher RH). In the next subsection, we formulate this process driven by both the electric field at the boundary and the number of oxyanions available (RH).

3.2. Rate of Incorporation of Oxyanions to the Boundary Oxide/Graphene

Under the assumption that a GO spot expands with radial symmetry by the incorporation of covalently attached oxyanions to the graphene preferably at the boundary with the oxidized zone, we propose a simple model to explain the evolution of the GO radius versus time, shown in Figure 3c.

First, the differential increment of oxyanions, d(OH$^-$), necessary to produce a differential increment or radius dr_b can be expressed as

$$d\left(OH^-\right) = \frac{2\pi r_b}{A_{OH}}dr_b \tag{5}$$

where A_{OH} is the effective area of an oxyanion.

Second, the probability that one oxyanion close to the boundary incorporates to graphene, P_{1OH}, depends essentially on an energetic barrier to overcome (W). This probability can be formulated according to the classical Boltzmann statistics. A reduction of the energetic barrier due to the influence of the neighboring electric field should be also included. In fact, when a negative potential is applied to the probe respect to graphene, the dielectric GO generates a negative polarization charge density at its outer edge, which in turn attracts a mirror positive charge in the p-type graphene. The attraction between this positive charge and the negatively charged oxyanions from the environment is considered the driving force for their incorporation to the graphene. Then, under an external voltage, P_{1OH} is expressed as

$$P_{1OH} = Ke^{-\frac{(W - er_{ef}E_{GO}(r_b))}{kT}} = \tilde{K}e^{\tilde{\alpha}E_{GO}(r_b)} \tag{6}$$

where the energy barrier W is measured in kT units (k, Boltzmann constant, and T the absolute temperature), K is a factor measured in s^{-1} and W is reduced by the kinetic term $e \cdot r_{ef} \cdot E_{GO}(r_b)$, where $E_{GO} = E(r_b)$ (as determined in the previous section), and r_{ef} is an effective displacement corresponding to the extension of the field at the boundary. Since no noticeable shrinkage of the spots has been detected in an interval of few days in dry ambient, the detaching probability is neglected for simplicity.

Third, the total rate of incorporated oxyanions d(OH$^-$)/dt can be described by the probability of attaching one oxyanion (P_{1OH}) multiplied by the number of possible sites (C atoms) along the entire spot perimeter (N_{OH}), and the probability of one site to be occupied (P_S) in terms of the density of available oxyanions around

$$\frac{d(OH)}{dt} = P_{1OH} \cdot N_{OH} \cdot P_S = P_{1OH} \cdot 2\pi r_b \cdot f(RH) \tag{7}$$

where the product $N_{OH} \cdot P_S$ can actually be expressed as the perimeter of the spot multiplied by a certain function f(RH) that ultimately depends on the relative humidity.

Note that in the previous equation we do not need to discuss about the source of oxyanions, either coming from a water bridge or wetting layer. By substituting (4) and (6) in (7), and taking advantage of the relation between (OH) and r_b in (5), a function t(ř) describing inversely the spot radius expansion along time is obtained by integration

$$t(\check{r}) = FC \int_1^{\check{r}} e^{-\frac{\tilde{a}}{\check{r}\ln(\check{r})}}d\check{r} \tag{8}$$

where expressions for parameters $\tilde{a}$ (nondimensional) and FC (measured in s) are described in the Supporting Information.

Equation (8) shows, in just one expression, an initial fast raising of ř with time, followed by a long slowdown, which precisely coincides with the experimental data behavior in Figure 3c. Those data are then least-square fitted to Equation (8), using $\tilde{a}$ and FC as fitting parameters. For the set of points recorded at $V_0 = -30$ V and RH = 95%, $\tilde{a} = 8.7$, and FC = 1.2, and for the points at RH = 90% $\tilde{a} = 6.9$, and FC = 2.6, giving rise to the trend solid curves of Figure 3c.

3.3. Formulation of the Electric Current Measured During Graphene Oxidation

Next, a formulation of the current during the oxidation process is proposed only for the aforementioned stage iii in Figure 4, corresponding to the measured decay of the current during GO expansion.

Assuming, for simplicity, that each oxyanion delivers one electron to the circuit when incorporates to graphene, the Faradaic or electrochemical component of the current (I_{EC}) is defined as $I_{EC} = e^- \, \text{d(OH)}/\text{d}t$. Which may be directly expressed as a function of the relative ř using Equations (5) and (6)

$$I_{EC} = e^- \frac{\text{d(OH)}}{\text{d}t} = \frac{\text{FD}}{\text{FC}} \check{r} e^{\frac{\tilde{a}}{\check{r} \ln(\check{r})}} \tag{9}$$

where $\text{FD} = (2e\pi \, r_0^2)/A_{OH}$. Some clarifications about the divergence of I_{EC} when $r \to \infty$ are discussed in the Supporting Information. Note that once determined the parameters FC and $\tilde{a}$ from the previous experiments, Equation (9) includes only an unknown factor, FD, which in turn depends exclusively on one unknown quantity, A_{OH}, the effective area of an oxyanion within the GO. Thus, determination of the single parameter FD in the I_{EC} expression provides the degree of oxidation of graphene.

The interpretation of the measured current requires considering at least two additional components: carrier transport across the oxide, and capacitive transient current. The transport or drift component would be an effect of the conductance in the GO insulator, mainly through the sites of non-oxidized graphene. Since in our model the decay of the current with time is considered a result of the oxide expansion, we will be fundamentally concerned with the dependence of the transport current on the increase of the spot radius. The classical formulation of the current across insulators of very low mobility in a parallel plate geometry, and with negligible injection barrier, was proposed by Mott and Gurney.[57] In a system with radial symmetry and plates separated by a distance $r_b - r_0$, like in Figure 6, the equivalent formalism delivers a dependence of the transport component I_T on the relative radius as

$$I_T\left(\check{r}\right) = I_0 \bigg/ \left(\check{r}\sqrt{\check{r}^2 - 1} - \ln\left(\check{r} + \sqrt{\check{r}^2 - 1}\right)\right)^2 \tag{10}$$

where I_0 acts as an unknown parameter with current units, in turn depending on carrier mobility, permittivity, and the square

of the applied voltage, analogously to how it was derived in ref. [57]. Recent investigations by Ortuño et al. on the electronic transport in 2D layers with high dielectric constants,[58] reveal the existence of a nonlocal conductivity, σ, with a dependence on distance L as $\sigma = \sigma_0 \exp(\gamma/L)$. In any case, we note that whatever the model, the transport current is expected to decay rapidly with the radius of the spot, until it becomes irrelevant, as concluded previously from the analysis of $Q(t)$ in Figure 5. Thus, although initially the contribution to the current of the drift component may be higher than the electrochemical one, the latter ends up dominating with time.

With respect to the influence of the capacitive current, measurements of the electrical response of the tip-GO-graphene structure against the application of square, low voltage pulses (<1 V), reveal a time response in the order of few μs, what indicates very small values of C (few nF). The contribution from the thin slab of GO, despite its high permittivity, is then not very relevant for the whole value of C in our system, and a significant contribution to $I(t)$ is discarded.

3.4. Evaluation of the Drift and Electrochemical Components of the Electric Current During Graphene Oxidation

As an example, we proceed to evaluate the drift and electrochemical current components during the expansion of the GO spots in Figure 5c. For that purpose, instead of using a least-square fit of I_{EC} and I_T expressions to the measured currents in order to determine the unknown parameters (FD in I_{EC}, and I_0 in I_T), we will obtain conditions to derive these parameters algebraically, from the analysis of the integrated current curves, $Q(t)$.

A preliminary least-square fit of Equation (8) to the evolution of the spot radii over time, for the specific sets of the three spots performed at −25 V (Figure 5c), and −40 V (Figure 5d), is performed to determine the corresponding FC and $\tilde{a}$ parameters for both sets, resulting: FC = 0.424 and $\tilde{a} = 6.05$ for −25 V, and FC 0.381 and $\tilde{a} = 4.7$ for −40 V. Note that these values are specific for each applied voltage and RH, and therefore differ from those declared in the previous subsection.

Then, we follow the guidelines of Equation (1) to propose a linear system of equations

$$Q_{EC}(t_1) + Q_T(t_1) + \Delta Q_{1,2} = Q_{EC}(t_2) + Q_T(t_2) \tag{11}$$

where Q_{EC} and Q_T are the numeric integrals of the Faradaic and drift currents, respectively, and $\Delta Q_{a,b}$ are the increments of charge from t_a to t_b derived from Figure 5. In consonance with the simplicity of our idealistic approach, we use Equation (10) for the transport component of the current.

Solving the linear system of equations resulting from (11), the following results are obtained: FD = $9.7e^{-4}$ μC and $I_0 = 7.96$ μA (for the set of spots performed at $V_0 = -25$ V, and RH = 92%), and FD = $9.2e^{-4}$ μC and $I_0 = 20.4$ μA (for the set of spots performed at $V_0 = -40$ V, and RH = 92%). Using these results, the current components I_{EC} and I_T, and the total simulated current ($I_{EC} + I_T$) are plotted in **Figure 7**, together with the overlapped experimental trace measured for these GO spots performed at −25 V. Since we have not used directly

ADVANCED
SCIENCE NEWS
www.advancedsciencenews.com
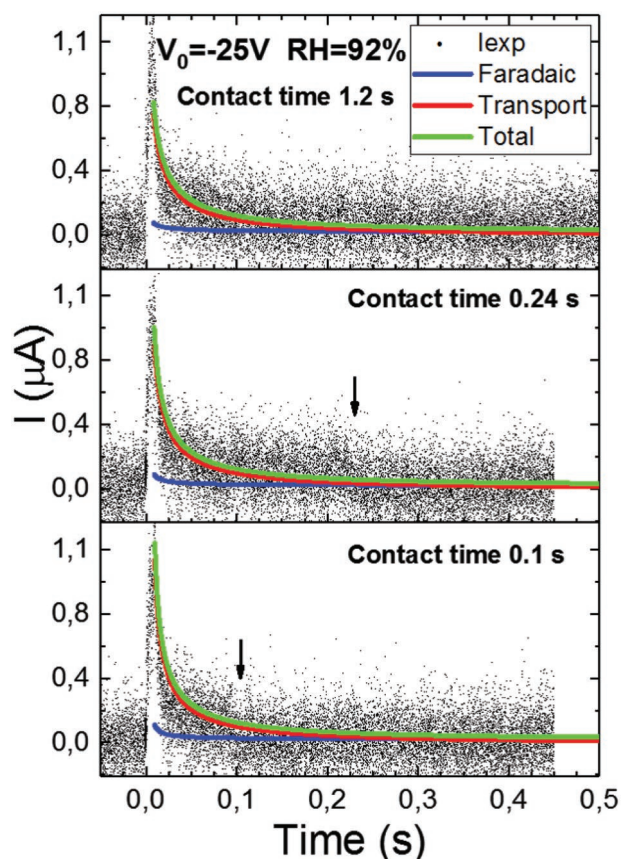
NANO · MICRO
small
www.small-journal.com

Figure 7. Experimental currents (dots) measured during oxidation of graphene at $V_0 = -25$ V, and RH = 92% keeping three different contact times. For each case, solid lines represent the predictions of the model proposed in this work. The red curve is the drift or transport component of the current; the blue curve is the electrochemical contribution, and the green is the sum of the previous ones. Arrows indicate the moment when the tip detaches from graphene.

keep between them a ratio very close to that of the square of the voltages (≈ 2.56), as predicted by the Mott–Gurney model. This very good agreement must be partly fortuitous, since the estimations of the charge increments $\Delta Q_{i,j}$ are not extremely fine. However, it encourages us to apply the aforementioned model to estimate the carrier mobility in GO which, for a relative dielectric permittivity in the range 10^4–10^5, should be in the order of 10^{-4}–10^{-5} cm^2 V^{-1} s^{-1}.

As it has been shown, RH is an important condition to determine the size of the GO spots, but does RH affect significantly the degree of oxidation inside the spots during their formation? In the model proposed, oxyanions are incorporated to the edge according to their steric factor and consequently the density should be uniform throughout the spot. Increasing RH only affects the rate for oxyanions incorporation, but not the degree of oxidation inside the spot. To check this aspect, we have used the qualitative information provided by Raman spectroscopy. In **Figure 8**a we show three different Raman spectra (A, B, C), each one averaging more than 7 spectra recorded from different points on three spots oxidized at $V_0 = -25$ V, under different RH conditions: 94% (spot A), 81% (spot B), and 69% (spot C). The detailed analysis of both ratios, the I_D/I_G intensities, and peak areas A_D/A_G (see the Supporting Information for details), suggest a very similar degree of oxidation, although slightly higher as increasing RH.[46,47,59] This means that, as the spot is expanding, additional oxyanions can incorporate into interstices within them. This possibility is not included in our previous formulation, but is not considered as significant as to rule out the model fundamentals.

As a proof of concept, Figure 8b shows a secondary-electron SEM picture of an extended area of GO in graphene transferred onto quartz, of 1×1 mm, created by overlapping individual spots separated 15 µm. Below this picture, an AFM image reveals the topography within the oxidized region, which appears somewhat more irregular (within a few nm) compared to that of individual spots, although this feature is considered less important when it comes to such large oxidized regions. This sample, and others reaching dimensions up to 2×2 mm, constitute a milestone for the generation of GO 2D regions. We highlight the controlled geometry and short time (a few tens of minutes) spent in this process, what promises interesting expectations for applications in large area substrates.

Information about the microstructure, including molecular bonds, was obtained by performing X-ray photoelectron spectroscopy (XPS) on a treated, compact region of 2×2 mm^2, definitely confirming the oxidation of graphene after treatment. Figure 8c,d shows XPS spectra of untreated (c) and treated (d) areas over the same CVD graphene layer on quartz substrate. The spectrum of the untreated area is the same, within error, as the spectrum recorded from a pristine sample (see Figure S11 in the Supporting Information), confirming that only treated areas show differences in chemical environment. The binding energy used in the model for C = C bond is 284.9 eV, as reported in the literature[60,61] (see the Supporting Information for details). The initial pristine graphene layer already contains some oxidized carbon as it is typically observed for graphene (Figure 8c).[62] A significant increment in the area of the peaks characteristic of oxidized carbon (hydroxyl, epoxy, carbonyl, and
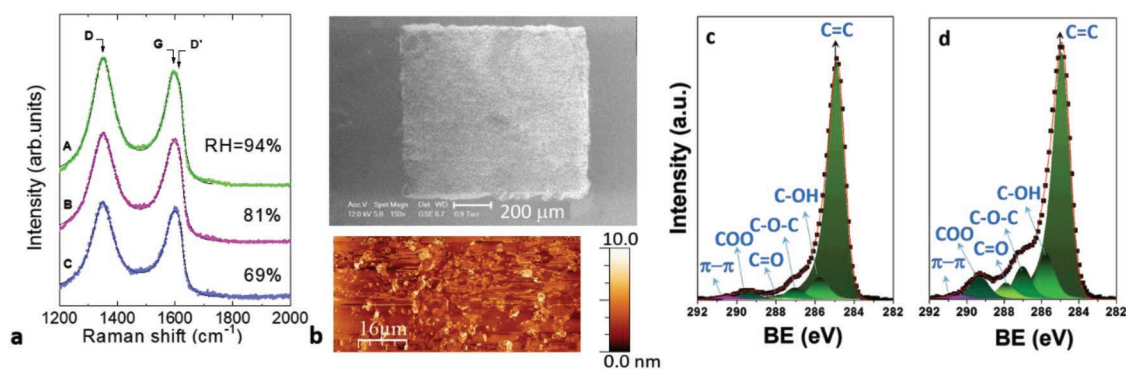
a fitting procedure to find the different components, but only an idealistic simple model combined with algebraic considerations, we consider it a good agreement. More refined models for the carrier transport in 2D insulators, such as that previously mentioned by Ortuño et al., could provide a more precise agreement.

These results allow verifying that the drift component I_T initially dominates the experimental current as previously suggested, but the electrochemical component I_{EC} ends up dominating from about 0.3 to 0.4 s onward. Results for the set performed at -40 V are shown in the Supporting Information.

According to the definition of FD in Equation (9), it is interesting to note that the derived values for this parameter correspond with estimated oxyanion areas of 0.026 nm^2 for the set at -25 V and 0.027 nm^2 for the one at -40 V, what implies a graphene fully oxidized in both cases. This is considered an overestimation, probably because not all the electrons delivered by the different oxygen–carbon bonds correspond to the incorporation of new oxygen, but also to the evolution of the initial hydroxyl bonds toward epoxy or carbonyl bonds, as will be described later. On the other hand, we find that the I_0 parameters derived above for both operating voltages, -25 and -40 V,

Figure 8. a) Average micro-Raman spectra recorded from the best quality regions of GO spots (excluding tip-affected center, and edge) performed at $V_0 = -25$ V and RH = A) 94%, B) 81%, and C) 69%. b) SEM image showing a region of 1×1 mm of graphene oxide obtained by overlapping individual spots of about 30 µm diameter (up), and AFM topographic image of a surface region within the square (down). c) C 1s spectrum of the untreated and treated d) area over the graphene sample showing the different carbon atoms determined in the surface.

carboxylic) can be observed in the spectrum from the oxidized area in Figure 8d. Oxidized carbon species increases two times after treatment, reaching a C/O ratio of about 2.85/1, somewhat lower as that reported for GO flakes obtained by the Hummers' method.

4. Conclusion

A novel and specific device performs a massive local anodic oxidation of graphene to produce high quality graphene oxide (GO) monolayers, with extension up to several mm², what constitutes a milestone in GO 2D monolayers. Large areas are obtained by overlapping individual spots, with diameters as large as 120 µm, achieving ratios $r_{GO}/r_0 > 10$ (where r_{GO} and r_0 are the GO disc and tip radius, respectively), unnoticed in previous LAO studies on other materials.

This scale is ideal to study in detail the mechanisms driving this process. Series of oxidized spots have been achieved with great reproducibility upon variation of different operating parameters: voltage, relative humidity, and exposure time. The large amount of charge involved in the formation of spots has allowed recording the transient current during anodic oxidation in the interval up to two seconds. The observations suggest that, under applied voltage, the giant permittivity of GO produces a high polarization charge just at the GO/graphene edge, which attracts free positive charge of the surrounding graphene (p-doped), and in turn generates a rebound of the radial electric field at the boundary. Such an intense field acts as driving force for the incorporation of oxyanions. This hypothesis overcomes the current paradigm for LAO, based on the creation of a water bridge, and has been formulated from first classical principles. The model satisfactorily predicts the nonlinear evolution of the spot radii with the operating voltage and exposure time, and establishes a general framework for the anodic oxidation of other 2D materials.

By interpreting the measured current with the previous model, we find that carrier transport across the oxide dominates the process initially, although from 0.3 to 0.4 s the electrochemical current ends up prevailing. Within the Mott–Gurney approach for transport in insulators, we have estimated the carrier mobility in GO about 10^{-4}–10^{-5} cm² V⁻¹ s⁻¹. In addition, just by a combination of electrical measurements and optical imaging we are able to determine the degree of oxidation reached by LAO, which results highly oxidized. XPS measurements on an area of 2×2 mm² confirm a degree of oxidation somewhat lower to that measured in GO by the modified Hummer's method.

5. Experimental Section

A specific actuator was set up that aimed at performing LAO, as well as microelectrical discharges, on layers of different conductive materials over large areas. The system is described elsewhere[63] (see also the Supporting Information) and includes the possibility to accurately control the approach of the probe to a substrate in XYZ direction with 0.05 µm step accuracy, and 1 µm reproducibility. It can be done at a maximum speed of 15 mm s⁻¹, what guarantees scalability within a total allowed trip of 10 cm. Details about the operating mode, the spring probe employed, and tip diameter are described in the Supporting Information. For operating voltages and distances similar to those used in AFM, electric fields are expected to be significantly lower, although surface irregularities at the tip may perturb this in a way difficult to estimate. In practice, work is performed at twice the typical voltage employed with nanoprobes in other reports.

The system included a power supply (0–100 V) and high-speed oscilloscope (1.5 GHz, 10 Gs s⁻¹) to monitor and record the electrical response during operation.

The system also features a plastic cover and internal cold vapor generator to hold stationary humidity conditions, including a computer monitored thermo-hygrometer sensor.

A commercial AFM system, from Nanotec, operating in ambient conditions, was employed to perform morphological and electrostatic characterization of single GO spots (see the Supporting Information).

Characterization in different regions inside the oxidized spots was carried out by micro-Raman Spectroscopy with a resolution of 0.7 µm, by DIC optical microscopy and SEM. The resulting oxidized species were identified by X-ray photoelectron spectroscopy (see the Supporting Information).

Most of the experiments were performed on CVD graphene single layers transferred onto quartz to minimize the influence of the substrate conductivity and reactivity, although graphene transferred on SiO₂/Si:p+ was also studied. The graphene layer was electrically grounded (via four silver paint dots at the sample corners), so it was expected that all the current will flow through it.

Conflict of Interest

The authors declare no conflict of interest.

[1] X. Luo, T. Qiu, W. Lu, Z. Ni, *Mater. Sci. Eng., R* **2013**, *74*, 351.
[2] A. T. Lawal, *Biosens. Bioelectron.* **2018**, *106*, 149.
[3] G. Bottari, M. Ángeles Herranz, L. Wibmer, M. Volland, L. Rodríguez-Pérez, D. M. Guldi, A. Hirsch, N. Martín, F. D'Souza, T. Torres, *Chem. Soc. Rev.* **2017**, *46*, 4464.
[4] L. Dong, J. Yang, M. Chhowalla, K. P. Loh, *Chem. Soc. Rev.* **2017**, *46*, 7306.
[5] R. Shi, H. Xu, B. Chen, Z. Zhang, L. M. Peng, *Appl. Phys. Lett.* **2013**, *102*, 113102.
[6] C. Thiele, A. Felten, T. J. Echtermeyer, A. C. Ferrari, C. Casiraghi, H. V. Löhneysen, R. Krupke, *Carbon* **2013**, *64*, 84.
[7] I. Bergmair, W. Hackl, M. Losurdo, C. Helgert, G. Isic, M. Rohn, M. M. Jakovljevic, T. Mueller, M. Giangregorio, E. B. Kley, T. Fromherz, R. Gajic, T. Pertsch, G. Bruno, M. Muehlberger, *Nanotechnology* **2012**, *23*, 335301.
[8] W. M. Wang, N. Stander, R. M. Stoltenberg, D. Goldhaber-Gordon, Z. Bao, *ACS Nano* **2010**, *4*, 6409.
[9] F. Torrisi, T. Hasan, W. Wu, Z. Sun, A. Lombardo, T. S. Kulmala, G. W. Hsieh, S. Jung, F. Bonaccorso, P. J. Paul, D. Chu, A. C. Ferrari, *ACS Nano* **2012**, *6*, 2992.
[10] P. He, B. Derby, *2D Mater.* **2017**, *4*, 021021.
[11] I. K. Moon, J. Lee, R. S. Ruoff, H. Lee, *Nat. Commun.* **2010**, *1*, 73.
[12] M. C. Morant-Miñana, J. Heidler, G. Glasser, H. Lu, R. Berger, N. Gil-Gonzalez, K. Müllen, D. M. De Leeuw, K. Asadi, *Mater. Horiz.* **2018**, *5*, 1176.
[13] M. Zhou, Y. Wang, Y. Zhai, J. Zhai, W. Ren, F. Wang, S. Dong, *Chem. – Eur. J.* **2009**, *15*, 6116.

[14] P. R. Unwin, A. G. Güell, G. Zhang, *Acc. Chem. Res.* **2016**, *49*, 2041.
[15] Z. Wei, D. Wang, S. Kim, S. Y. Kim, Y. Hu, M. K. Yakes, A. R. Laracuente, Z. Dai, S. R. Marder, C. Berger, W. P. King, W. A. De Heer, P. E. Sheehan, E. Riedo, *Science* **2010**, *328*, 1373.
[16] R. Trusovas, G. Račiukaitis, G. Niaura, J. Barkauskas, G. Valušis, R. Pauliukaite, *Adv. Opt. Mater.* **2016**, *4*, 37.
[17] R. Garcia, A. W. Knoll, E. Riedo, *Nat. Nanotechnol.* **2014**, *9*, 577.
[18] R. Garcia, R. V. Martinez, J. Martinez, *Chem. Soc. Rev.* **2006**, *35*, 29.
[19] R. García, M. Calleja, F. Pérez-Murano, *Appl. Phys. Lett.* **1998**, *72*, 2295.
[20] C. Albonetti, J. Martinez, N. S. Losilla, P. Greco, M. Cavallini, F. Borgatti, M. Montecchi, L. Pasquali, R. Garcia, F. Biscarini, *Nanotechnology* **2008**, *19*, 435303.
[21] M. S. Johannes, D. G. Cole, R. L. Clark, *Nanotechnology* **2007**, *18*, 345304.
[22] L. Filipovic, S. Selberherr, *Microelectron. Eng.* **2013**, *107*, 23.
[23] P. Avouris, T. Hertel, R. Martel, *Appl. Phys. Lett.* **1997**, *71*, 285.
[24] E. Dubois, J. L. Bubendorff, *J. Appl. Phys.* **2000**, *87*, 8148.
[25] N. Cabrera, N. F. Mott, *Rep. Prog. Phys.* **1949**, *12*, 163.
[26] L. Zitzler, S. Herminghaus, F. Mugele, *Phys. Rev. B* **2002**, *66*, 1.
[27] E. M. Stuve, *Chem. Phys. Lett.* **2012**, *519–520*, 1.
[28] M. Bartošík, D. Škoda, O. Tomanec, R. Kalousek, P. Jánský, J. Zlámal, J. Spousta, P. Dub, T. Šikola, *Phys. Rev. B* **2009**, *79*, 1.
[29] M. Calleja, M. Tello, R. García, *J. Appl. Phys.* **2002**, *92*, 5539.
[30] R. Kumar, R. K. Singh, D. P. Singh, E. Joanni, R. M. Yadav, S. A. Moshkalev, *Coord. Chem. Rev.* **2017**, *342*, 34.
[31] A. Ladrón-de-Guevara, A. Boscá, J. Pedrós, E. Climent-Pascual, A. de Andrés, F. Calle, J. Martínez, *Appl. Surf. Sci.* **2019**, *467–468*, 691.
[32] H. Kuramochi, F. Pérez-Murano, J. A. Dagataand, H. Yokoyama, *Nanotechnology* **2004**, *15*, 297.
[33] E. S. Snow, G. G. Jernigan, P. M. Campbell, *Appl. Phys. Lett.* **2000**, *76*, 1782.
[34] J. A. Dagata, F. Perez-Murano, C. Martin, H. Kuramochi, H. Yokoyama, *J. Appl. Phys.* **2004**, *96*, 2386.
[35] M. C. Chuang, H. M. Chien, Y. H. Chain, G. C. Chi, S. W. Lee, W. Y. Woon, *Carbon* **2013**, *54*, 336.
[36] M. Munz, C. E. Giusca, R. L. Myers-Ward, D. K. Gaskill, O. Kazakova, *ACS Nano* **2015**, *9*, 8401.
[37] A. J. M. Giesbers, U. Zeitler, S. Neubeck, F. Freitag, K. S. Novoselov, J. C. Maan, *Solid State Commun.* **2008**, *147*, 366.
[38] L. Weng, L. Zhang, Y. P. Chen, L. P. Rokhinson, *Appl. Phys. Lett.* **2008**, *93*, 093107.
[39] T. F. D. Fernandes, A. C. Gadelha, A. P. M. Barboza, R. M. Paniago, L. C. Campos, P. S. Soares Guimarães, P. L. de Assis, B. R. A. Neves, *2D Mater.* **2018**, *5*, 025018.
[40] A. I. Dago, Y. K. Ryu, F. J. Palomares, R. Garcia, *ACS Appl. Mater. Interfaces* **2018**, *10*, 40054.
[41] I. S. Byun, D. Yoon, J. S. Choi, I. Hwang, D. H. Lee, M. J. Lee, T. Kawai, Y. W. Son, Q. Jia, H. Cheong, B. H. Park, *ACS Nano* **2011**, *5*, 6417.
[42] K. Zhang, Q. Fu, N. Pan, X. Yu, J. Liu, Y. Luo, X. Wang, J. Yang, J. Hou, *Nat. Commun.* **2012**, *3*, 1194.
[43] S. Ko, S. J. Lee, M. Son, D. Ahn, S.-W. Lee, *J. Korean Phys. Soc.* **2015**, *66*, 617.
[44] E. Climent-Pascual, M. García-Vélez, Á. L. Álvarez, C. Coya, C. Munuera, X. Díez-Betriu, M. García-Hernández, A. De Andrés, *Carbon* **2015**, *90*, 110.
[45] J. F. Rodriguez-Nieva, E. B. Barros, R. Saito, M. S. Dresselhaus, *Phys. Rev. B* **2014**, *90*, 1.
[46] X. Díez-Betriu, S. Álvarez-García, C. Botas, P. Álvarez, J. Sánchez-Marcos, C. Prieto, R. Menéndez, A. De Andrés, *J. Mater. Chem. C* **2013**, *1*, 6905.
[47] K. N. Kudin, B. Ozbas, H. C. Schniepp, R. K. Prud'homme, I. A. Aksay, R. Car, *Nano Lett.* **2008**, *8*, 36.

[48] O. Kazakova, V. Panchal, T. Burnett, *Crystals* **2013**, *3*, 191.

[49] S. S. Datta, D. R. Strachan, E. J. Mele, A. T. Charlie Johnson, *Nano Lett.* **2009**, *9*, 7.

[50] C. Gómez-Navarro, F. J. Guzmán-Vázquez, J. Gómez-Herrero, J. J. Saenz, G. M. Sacha, *Nanoscale* **2012**, *4*, 7231.

[51] Y. Shen, Y. Wang, Y. Zhou, C. Hai, J. Hu, Y. Zhang, *Beilstein J. Nanotechnol.* **2018**, *9*, 1146.

[52] R. L. McCarley, S. A. Hendricks, A. J. Bard, *J. Phys. Chem.* **1992**, *96*, 10089.

[53] J. Liu, D. Galpaya, M. Notarianni, C. Yan, N. Motta, *Appl. Phys. Lett.* **2013**, *103*, 1.

[54] P. Cudazzo, I. V. Tokatly, A. Rubio, *Phys. Rev. B: Condens. Matter Mater. Phys.* **2011**, *84*, 1.

[55] L. V. Keldysh, *JETP Lett.* **1979**, *29*, 658.

[56] K. S. Kumar, S. Pittala, S. Sanyadanam, P. Paik, *RSC Adv.* **2015**, *5*, 14768.

[57] N. F. Mott, R. W. Gurney, *Electronic Processes in Ionic Crystals*, Oxford University Press, London **1940**.

[58] M. Ortuño, A. M. Somoza, V. M. Vinokur, T. I. Baturina, *Sci. Rep.* **2015**, *5*, 1.

[59] S. D. M. Brown, A. Jorio, P. Corio, M. S. Dresselhaus, G. Dresselhaus, R. Saito, K. Kneipp, *Phys. Rev. B: Condens. Matter Mater. Phys.* **2001**, *63*, 1.

[60] A. Kovtun, D. Jones, S. Dell'Elce, E. Treossi, A. Liscio, V. Palermo, *Carbon* **2019**, *143*, 268.

[61] S. Huh, J. Park, Y. S. Kim, K. S. Kim, B. H. Hong, J. M. Nam, *ACS Nano* **2011**, *5*, 9799.

[62] Z. Li, Y. Wang, A. Kozbial, G. Shenoy, F. Zhou, R. McGinley, P. Ireland, B. Morganstein, A. Kunkel, S. P. Surwade, L. Li, H. Liu, *Nat. Mater.* **2013**, *12*, 925.

[63] Á. L. Álvarez, C. Coya, M. García-Vélez, *Rev. Sci. Instrum.* **2015**, *86*, 084704.